

Ultraviolet Metasurfaces of $\approx 80\%$ Efficiency with Antiferromagnetic Resonances for Optical Vectorial Anti-Counterfeiting

Kun Huang, Jie Deng, Hai Sheng Leong, Sherry Lee Koon Yap, Ren Bin Yang, Jinghua Teng, and Hong Liu*

Metasurfaces enable the full control of electromagnetic waves over a wide spectrum. High-efficiency transmissive metasurfaces have been demonstrated up to the visible frequencies by using dielectrics. However, extending the operating spectrum to the ultraviolet range is challenging. This is due to the strong absorption in typical dielectric materials and the inexhaustive understanding of the magnetic resonances in dielectric nanostructures. Here, a large-bandgap material—niobium pentoxide (Nb_2O_5)—is introduced to engineer the ultraviolet geometric meta-holograms to achieve a total efficiency of 79.6% at 355 nm wavelength. The employed orientation-varying nanobricks, operating as miniaturized half-waveplates (HWPs), are elaborately designed to excite the antiferromagnetic modes that maintain E_x component of the incident light via even antiparallel magnetic dipoles (AMDs) but reverse E_y component via odd AMDs, thereby unveiling the underlying mechanism of dielectric nano-HWPs. By adding the polarization degree of freedom, an ultra-channel meta-hologram, multiplexing two orthogonal spin channels while exhibiting three outputs, is demonstrated experimentally for ultraviolet vectorial anti-counterfeiting. This work might open the door toward high-performance ultraviolet nanophotonics and meta-optics.

their traditional counterparts, they also possess some unprecedented properties such as polarization sensitivity^[16,17] and nonlinear effects.^[18,19] High-efficiency manipulation of light is the cornerstone of many potential applications of metasurfaces. Metal-based metasurfaces which rely on plasmonic resonances can achieve an efficiency of $\approx 80\%$ in the visible and near-infrared ranges^[8,20] in the reflective mode. In the transmission mode, however—the preferred mode in many devices and systems—these metasurfaces have a low transmission efficiency.^[9,21,22] In contrast, the low-loss dielectric metasurfaces employing magnetic resonances^[15,22] are promising candidates. Silicon metasurfaces have an efficiency of $\approx 80\%$ to 90% in the near-infrared range,^[9,23] while titanium oxide (TiO_2),^[2,11] gallium nitride (GaN),^[24] and silicon nitride (Si_3N_4)^[25] metasurfaces have outstanding performance at the visible wavelengths.

Hitherto, the reported ultraviolet metasurfaces suffer from low efficiency as

1. Introduction

As subwavelength-pixel diffractive optical elements, metasurfaces could tailor the phase and amplitude of the reflected and transmitted light by tuning the geometry of structures.^[1–7] Not only do metadevices such as meta-holograms,^[8–10] metalenses,^[11–14] and metagratings^[15] realize the functionalities of

they pose rigorous requirements on material properties such as low loss, high refractive index, and manufacturability of nano-patterning in ultra-small pixel pitches. Photon-sieve holograms^[26] perforated in metal films have been reported at ultraviolet wavelengths,^[27] but the low efficiency restricts their general applications. Due to the small bandgap, silicon-based ultraviolet metasurfaces^[28] have experimental efficiencies below 30%. Therefore, developing a novel material platform would enable metasurfaces to contribute to the ultraviolet region.^[29]

Moreover, although both electric and magnetic resonances could be observed in dielectric nanostructures,^[30] their roles in tailoring optical properties of some structures have not been investigated comprehensively. Taking the dielectric geometric metasurfaces, for example, magnetic multipole resonances^[21] dominate the orientation-varying nanofins, functioning as nanoscale half-waveplates (HWPs),^[16] which could modulate the geometric phase of circularly polarized (CP) transmitted light. In principle, the magnetic multipolar interference can be used to describe the electromagnetic scattering of nanostructures^[31] but it cannot provide a clear explanation about the phase delay of

Prof. K. Huang


Department of Optics and Optical Engineering
University of Science and Technology of China
Hefei 230026, Anhui, China

Prof. K. Huang, Dr. J. Deng, Dr. H. S. Leong, Dr. S. L. K. Yap, Dr. R. B. Yang, Prof. J. Teng, Dr. H. Liu

Institute of Materials Research and Engineering
Agency for Science

Technology and Research (A*STAR), 2 Fusionopolis Way, #08-03,
Innovis, Singapore 138634

E-mail: h-liu@imre.a-star.edu.sg

 The ORCID identification number(s) for the author(s) of this article can be found under <https://doi.org/10.1002/lpor.201800289>

DOI: 10.1002/lpor.201800289

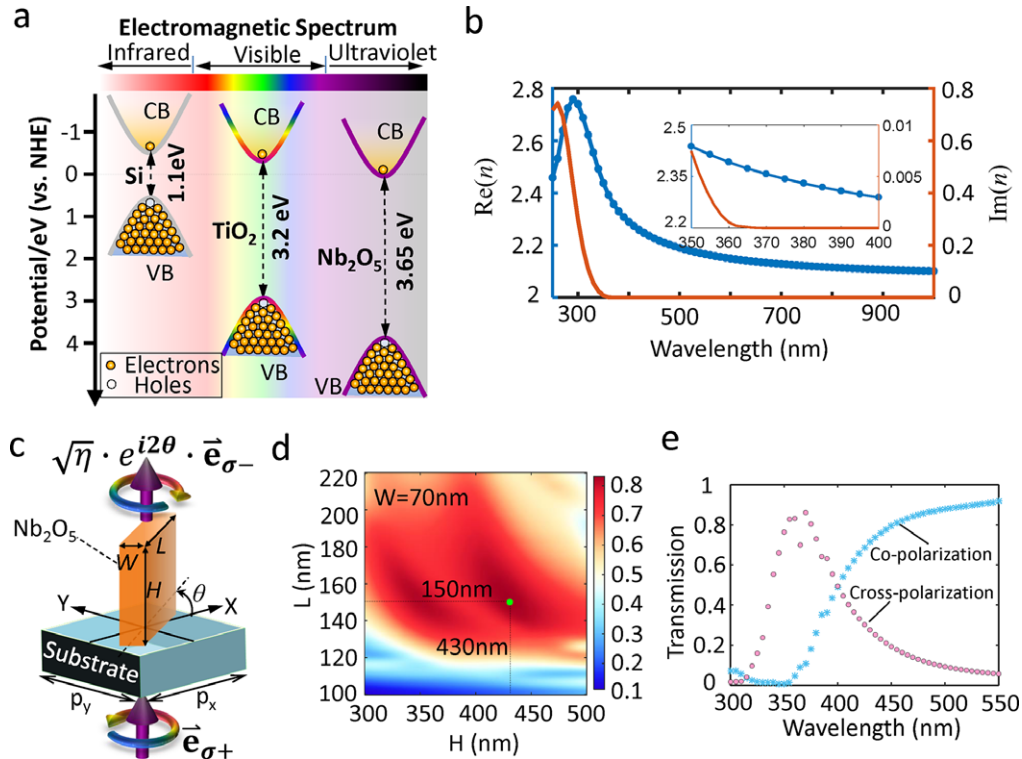


Figure 1. Nb₂O₅-based metasurfaces. a) The bandgap diagram of silicon (Si), titanium dioxide (TiO₂), and niobium pentoxide (Nb₂O₅) at infrared, visible, and ultraviolet spectra, respectively. The potentials are with respect to normal hydrogen electrode (NHE). The conduction (CB) and valence bands (VB) of electron in materials are sketched by colored curves. b) Measured complex refractive index of our ALD-grown Nb₂O₅ film. c) Sketch of a cell unit with the dimension of $p_x = p_y = 250$ nm. The Nb₂O₅ nanobrick with a rotation angle of θ is located on a quartz substrate and used to convert the incident circular polarization into the transmitted cross-polarization with efficiency η and an additional phase modulation of $e^{i2\theta}$. d) Simulated conversion efficiency η for nanobricks with a fixed width of 70 nm and various heights H and lengths L . The peak efficiency of $\approx 83\%$ is located at $W = 70$ nm, $H = 430$ nm, and $L = 150$ nm. The simulation is carried out in FDTD by using the measured refractive index in (b). e) Broadband response of the optimized nano-brick array. In the transmitted light, the efficiency values are shown by addressing the co-polarization and cross-polarization parts relative to incident polarization. The co-polarization transmitted light has no phase modulation.

π between two orthogonal components of the incident electric field.

To address these challenges, we develop dielectric geometric metasurfaces at the ultraviolet wavelengths by employing Nb₂O₅ nanobricks that are designed to support the antiferromagnetic resonances. Theoretically, we find that antiferromagnetic modes with even and odd antiparallel magnetic dipoles (AMDs) are induced by x - and y -components of the incident circular polarization light, respectively. The even AMDs can maintain the electric vectors of light at the input and output planes of nanobricks, while the odd AMDs inverse both electrical vectors, thus realizing the polarization conversion between two spins. Due to the large bandgap and high refractive index, a conversion efficiency of $\approx 83\%$ is predicted to convert the incident circular polarization light into the transmitted cross-polarized light via Nb₂O₅-based geometric metasurfaces operating at the wavelength of 355 nm. A transmissive meta-hologram has been demonstrated experimentally with a total efficiency as high as 79.6% and a large angle of view of $\approx 64^\circ$. As a proof-of-concept demonstration of ultraviolet vectorial anti-counterfeiting, we design and fabricate an ultra-channel meta-hologram that encodes two spin channel sparse holograms while generating three different images with

polarization features. This provides a new approach for optical encryption and security.

2. Results and Discussion

2.1. Material Platform

Nb₂O₅ has a bandgap of ≈ 3.65 eV (see **Figure 1a**), which is ≈ 0.45 and ≈ 2.55 eV higher than TiO₂ and silicon, respectively. Its relatively large bandgap determines that Nb₂O₅ exhibits a wide transparency window spanning the ultraviolet, visible, and infrared regions.^[32] The intriguing properties of high-permittivity and low-absorption enable many applications in solar cells^[33] and light-emitting-diodes.^[34] Moreover, the Nb₂O₅ films can be manufactured by general deposition techniques and synthesized into various shapes.^[32] In this work, atomic layer deposition (ALD) method^[35] is employed to prepare the amorphous Nb₂O₅ at a temperature of 90 °C. This temperature is purposely chosen to be below the glass-liquid transition temperature of the electron beam lithography resist to ensure high-fidelity pattern transfer. The as-grown Nb₂O₅ film has a refractive index of 2.2 ($\text{Re}(n)$), and

a negligible extinction ratio ($\text{Im}(n)$) at the ultraviolet wavelengths ranging from 350 to 400 nm (Figure 1b). The refractive index and the extinction ratio were measured with an ellipsometer.

2.2. Metasurface Design

Figure 1c sketches one unit cell of the orientation-rotating Nb_2O_5 nanobricks on quartz. For the left-handed CP light of incidence, one part of its transmitted light is converted into the right-handed circular polarization and simultaneously obtains an additional phase that is twice of the rotation angle θ . The simulation is implemented by using the finite-difference time-domain method in a commercial software, Lumerical. The computational area is set to be $250 \times 250 \times 2000$ nm in x , y , and z directions, respectively. To investigate the optical response of the periodic nanostructures, periodic boundary conditions are employed along the x and y directions, while perfectly matched layers are used along the z directions to eliminate the unwanted reflections from the top and bottom of the calculation window. To fully map the conversion efficiency over different geometry of the nanobricks, an algorithm was developed to re-call the main program by changing the geometric parameters of nanobricks in every loop. Considering the fabrication limits, we set the width of nanobrick to be $W = 70$ nm, which is achievable with our electron-beam lithography (EBL). Figure 1d shows the simulated efficiency with the length varying from 100 to 220 nm and the height from 300 to 500 nm. The simulated efficiency is calculated by using the ratio of the transmitted light with cross polarization to the total incident light. It can be seen that the peak efficiency of $\approx 83\%$ is attainable with $L = 150$ nm and $H = 430$ nm. In addition, the neighboring geometries also exhibit an efficiency of $>80\%$, thereby allowing a large tolerance to the fabrication error.

Figure 1e shows the simulated efficiency at wavelengths from 300 to 550 nm. The efficiency of the transmitted light with cross-polarization is $\approx 80\%$ near the designed wavelengths of 355 nm and decreases as the wavelength deviates. For the efficiency larger than 50%, the simulated bandwidth is ≈ 60 nm ranging from 340 to 400 nm. In addition, the total transmission (including co-polarization and cross-polarization light) is above 80% when the wavelength is larger than 350 nm, which implies that the Nb_2O_5 nanostructures with an optimized geometry could also work as high-efficiency visible light metasurfaces.

2.3. Antiferromagnetic Resonances

For transmissive geometric metasurfaces, realizing high conversion efficiency requires two conditions: high transmission of both electric fields and phase delay of π between the orthogonal electric field components. It has been reported that both electric and magnetic responses must simultaneously exist in the meta-structures for realizing high transmission.^[36] In the dielectric nanostructures where the electric currents are absent, the electromagnetic resonances come from the electric displacement currents and their induced magnetic fields, which therefore hold promise for high transmission through their interference or coupling.

To unveil the mechanism behind the phase delay of π , we introduce the antiferromagnetic resonances, where a series of staggered magnetic dipole modes are excited with antiparallel orientations. This antiferromagnetic resonance mode usually exists in layered magnetic structures^[37] that are used for information storage. This mode is also investigated to probe the connection between antiferromagnetic spintronics and topological structures.^[38,39] Recently, 1D antiferromagnetic chain has also been observed in other artificially engineered structures such as the plasmonic nanodisk array^[40] and hybrid metamaterials.^[41,42] To show its role in our case, we investigate both electric and magnetic fields resonating in the optimal nanobrick (see Figure 2a,b). For the E_x component, its induced electric fields contain four circle displacement currents with alternative clockwise and anti-clockwise directions, which are aligned to four AMDs that are vertically located along the z axis. In these antiferromagnetic modes, the even circle currents orientate both electric vectors of light at the incident (bottom) and output (top) ends of the nanobrick in the same direction (see Figure 2a). It implies that the x -component of the incident CP light is maintained after passing through nanobricks. However, for E_y component, an antiferromagnetic mode with three AMDs is induced, so that these odd circle displacement currents make the electric vector of the transmitted light inverse to that of incident light (Figure 2b), indicating a phase delay of π . Thus, the transmitted light has its polarization completely orthogonal to the incident light, manifesting a high-efficiency polarization conversion.

Two coupling effects dominate the interaction between the nanobricks and the antiferromagnetic modes. The first coupling arises from the fact that, the dimension of nanobricks determines the number of the magnetic dipoles existing in each antiferromagnetic mode induced by E_x - or E_y -component. The long axis (x -axis in Figure 2b) of the nanobricks allows these x -orientated magnetic dipoles to oscillate in a large volume. Contrarily, a magnetic dipole oscillating along the y axis (Figure 2a) has a small volume, which is constrained by the 70 nm width. Since the geometry of nanobricks are fixed, the number of x -orientated magnetic dipoles (Figure 2b) is 1 less than that of y -orientated magnetic dipoles (Figure 2a). Consequently, the even and odd AMDs, oscillating along the x and y axes respectively, are excited simultaneously for the polarization conversion. Second, the magnetic dipole coupling in an antiferromagnetic mode influences the weight of every dipole. The dipole-coupled method (see Section S1, Supporting Information) is used here to calculate their coupling weights. Using the AMDs induced by the single-ring displacement currents, we mimic the antiferromagnetic modes (Figures 2c,d), where each dipole has a different weight. As expected, the even (odd) dipole modes maintain (reverse) the electric vector of the incident light, which provides a theoretical proof for the antiferromagnetic resonances existing in dielectric nanobricks.

2.4. High-Efficiency Ultraviolet Meta-Holograms

To validate the efficiency, a meta-hologram as sketched in Figure 3a is proposed to modulate the cross-polarized transmitted light with a position-dependent phase (Figure 3b) for reconstructing a “rabbit” image (Figure 3c) at 355 nm wavelength. The proposed meta-hologram is a Fresnel hologram that

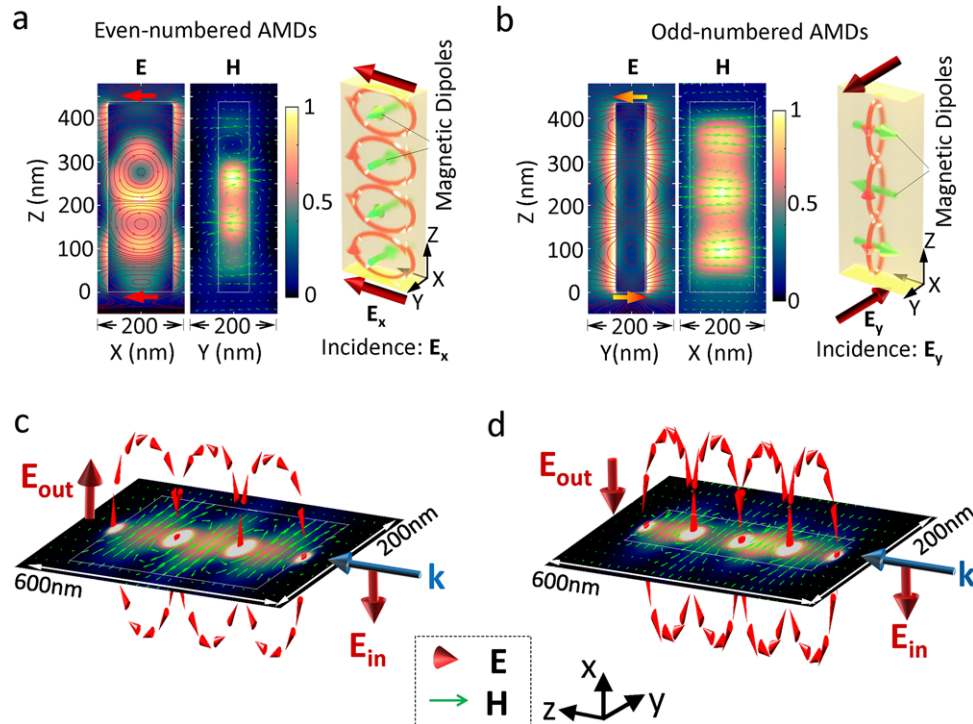


Figure 2. Optical antiferromagnetic resonances in geometric metasurfaces. a,b) Total electric (E) and magnetic (H) fields existing in the optimized nanobrick when it is excited by x -polarized (a) and y -polarized (b) incident light. The vector profiles of induced electric and magnetic fields are distinguished by using the red lines and green arrows, respectively. The white rectangles denote the boundaries of nanobrick. The vertically staggered magnetic dipole moments in an anti-parallel alignment, that is, anti-ferromagnetic modes, are excited and confined within the nanobrick. The anti-ferromagnetic modes with even (a) and odd (b) dipole moments are induced by E_x and E_y components of the incident light, respectively. The insets show the simplified sketches of two antiferromagnetic modes. c,d) The antiferromagnetic modes composed of the odd (c) and even (d) anti-parallel magnetic dipoles that are induced by single-ring currents (taken as the approximation of optically induced volume currents in (a,b)). The vectors of single-ring currents are represented by 3D red arrows. The coupling weight of every magnetic dipole is calculated by using the dipole-couple method. To simplify our simulation, all the single-ring currents have the same radius of $430 \text{ nm}/(2N)$, where N is the number of magnetic dipoles.

has its imaging plane located at the meso-field of $300 \mu\text{m}$, as shown in Figure 3a. An accurate simulation of its propagation in free space can be implemented by using Rayleigh–Sommerfeld diffraction integral, which is realized by using our developed method based on the fast Fourier transform.^[43] This numerical Rayleigh–Sommerfeld diffraction shows a better accuracy than the angular spectrum method, in which the evanescent frequencies contained in the metasurface-modulated optical fields are dropped and therefore lead to inevitable errors. To design the hologram, a modified Gerchberg–Saxton (GS) algorithm^[21] is used to determine the required phase (Figure 3b) for reconstructing a “rabbit” image in Figure 3c. To avoid the diffraction loss, the designed phase is discretized into 16 levels (with a phase value $\varphi_n = 2\pi n/16$ at the level n), which correspond to the nanobrick with an angle $\theta = \varphi_n/2$. In addition, we have to point out that the speckles in the simulated image can be suppressed by increasing the total size of meta-hologram (see Section S6, Supporting Information), which will be difficult to fabricate.

Experimentally, the hologram is fabricated by using the electron beam lithography and ALD technique (see Section S2, Supporting Information). Figure 2d shows its scanning electron microscope (SEM) images with nearly-vertical side walls, indicating a precisely patterned device. More SEM images with larger field of view can be found in Figure S3, Supporting Information.

The experimental setup is built in a confocal microscope (see Section 3, Supporting Information). A weakly focused CP light is used to increase the incident power on the hologram, and its transmitted light is collected by an objective lens and then recorded by a charge-coupled device (CCD) camera, without using polarization analyzer. Figure 3e displays the captured image with a clear contour and high signal-to-noise ratio. The image is also immune to twin image and high-order diffractions. The root-mean-square error (RMSE) between the experimental and ideal image is calculated to be $\approx 32.3\%$, which has the deviation with the simulated value of 11.6% . This discrepancy might be caused by the inevitable fabrication error and the weakly focused incident beam with a Gaussian profile that differentiates from the theoretical assumption of a uniformly distributed plane wave. In addition, a quantitative comparison between the experimental and simulated line-scanning intensity profiles is shown in Figure 3f, indicating a similar contour.

To determine its total efficiency, we experimentally take the light shining within the hologram area of $100 \times 100 \mu\text{m}$ as the total incidence (I_{in}). The output (I_{out}) is evaluated by the power encircled only in the “rabbit” pattern, excluding any background noise (see Section 4, Supporting Information). Considering that our hologram has an imaging plane of $z = 300 \mu\text{m}$, the image power cannot be measured directly by using a power meter. In

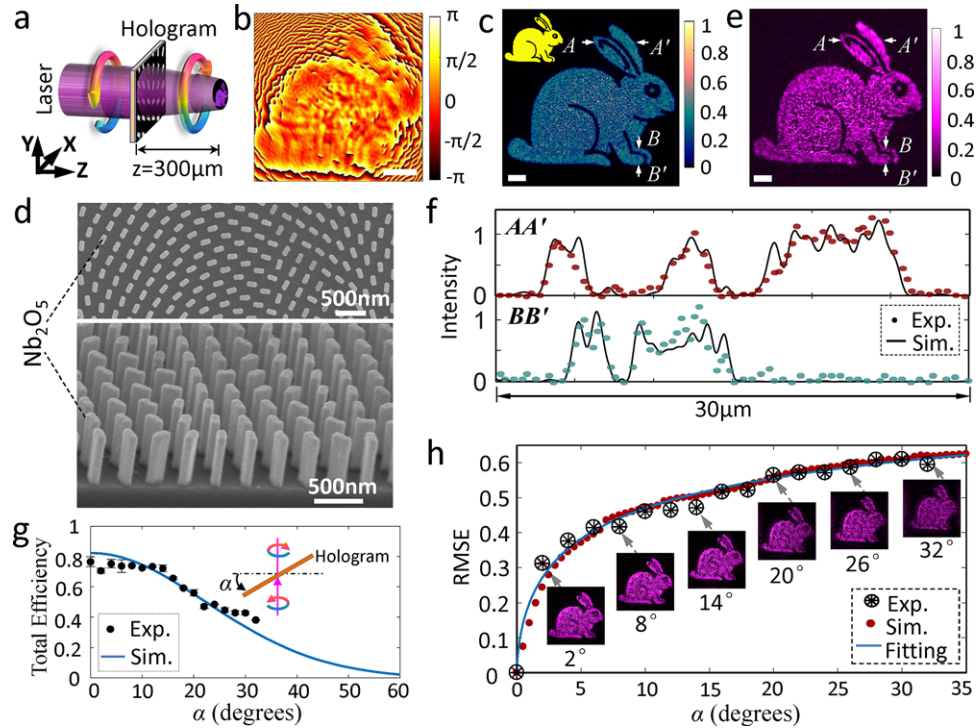


Figure 3. Ultraviolet meta-hologram. a) Working principle of this meta-hologram converting the left-handed circular polarized light into the right-handed one and reconstructing a holographic image at a distance of $z = 300 \mu\text{m}$. The circular arrows represent the left- (before the hologram) and right-handed (after the hologram) CP light, respectively. b) The designed phase profile with a size of $100 \times 100 \mu\text{m}$ and pixel pitch of $250 \times 250 \text{ nm}$. The lines AA' and BB' denote the locations of line-scanning intensity profiles for data analysis. c) Simulated holographic image with a pattern of "rabbit," whose ideal image is shown in the inset. Scale bar: $10 \mu\text{m}$. d) SEM images of our fabricated samples with top (upper) and tilting (lower, 60°) view. Scale bar: 500 nm . e) Captured holographic image by CCD camera. Scale bar: $10 \mu\text{m}$. f) Simulated and measured 1D intensity profiles along the lines with their locations denoted by AA' and BB' in (c) and (e). g) Simulated and measured efficiency at different incident angles ranging from 0° to 60° . Due to the sufficient phase level of 16, all the modulated cross-polarized light is considered to contribute to the holographic image. Therefore, the simulation data (solid curve) obtained directly from FDTD calculations can be taken as the theoretical total efficiency. The simulated efficiency by FDTD is obtained by changing the angle between the optical axis (z-axis) and the wave vector of incident CP light. The inset shows the sketch of realizing the oblique incidence by tilting the hologram. h) RMSEs of images between the normal and oblique incidence. Simulated RMSEs are represented by red dots and fitted by a solid curve while experimental results are shown by encircled asterisks. The insets show several experimentally captured images taken under incidence angles with an interval of 6° .

our experiment, the intensity profiles of incident light and the holographic image are captured in gray scale by using a CCD camera, without any data saturation for avoiding experimental error of the intensity recording. The experimental ratio $I_{\text{out}}/I_{\text{in}}$ is measured as high as 80.8%. In order to remove the contribution from the co-polarized light, the ratio of the cross-polarization part to the co-polarized one in the transmitted light is experimentally measured with a value of 16. Considering that only one part (i.e., 23.34%) of the co-polarized light is encircled in the rabbit pattern, we can mathematically derive the contribution from the co-polarized light, which is calculated as 1.2%. Thus, the total efficiency from the purely cross-polarized light is 79.6%. To the best of our knowledge, it is the highest efficiency in the ultraviolet metasurfaces ever reported and comparable to those for metasurfaces at the visible and infrared wavelengths.^[8,9,23]

Conversion efficiency and image quality of this hologram are investigated under oblique illumination. The oblique incidence is realized by tilting the sample that is fixed onto a rotation mount for recording the angle α (see the inset in Figure 3g). After removing the contribution from the co-polarized light, the measured results in Figure 3g have a good agreement with the simulated

ones. The efficiency decreases with the increasing α , which originates from the reduction of z-component of the wave-vector and the enlarged reflection from the sample substrate. Similarly, the uniformity and shape of the holographic images deteriorate upon increasing α , as observed in Figure S5, Supporting Information. To evaluate its fidelity, the RMSEs of the images taken under the oblique and normal illuminations are calculated and plotted in Figure 4c, where both RMSEs agree well. It shows that the image fidelity deteriorates when RMSE increases with the incidence angle α . We note that the image pattern at $\alpha = 32^\circ$ is still distinguishable, which implies a large angle of view of $64^\circ \times 64^\circ$.

2.5. Ultraviolet Vectorial Anti-Counterfeiting

Traditionally, optical holographic anti-counterfeiting devices by using microstructures cannot respond to the polarization of ultraviolet light. To enhance the security level via polarization, we design an ultra-channel meta-hologram consisting of two orthogonal channels that could encode two spin-dependent sparse holograms (see Figure 4a), sharing a square-shaped aperture.^[20] Upon

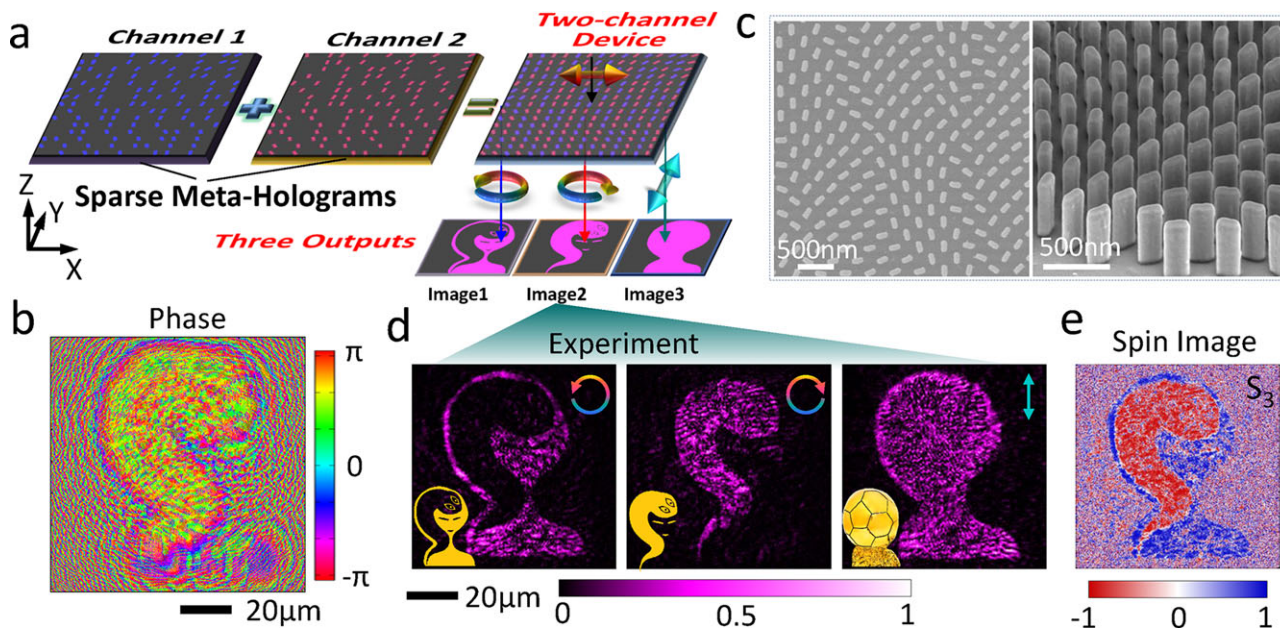


Figure 4. Ultra-channel meta-holograms. a) Sketch of ultra-channel hologram composed of two sparse meta-holograms sharing a square aperture of $100 \times 100 \mu\text{m}$. The nanobricks in both sparse meta-holograms are randomly distributed. The sparse meta-holograms 1 and 2 operate for right- and left-handed circular polarizations and generate two complementary images of “girl” and “snake” at a target cut plane of $z = 200 \mu\text{m}$ from the hologram plane. b) Combined phase profiles encoded in both sparse meta-holograms. c) SEM images of our fabricated hologram in top (left) and tilting (right) view. d) Measured holographic images under different polarization analyzers. The insets at the bottom-left corner display their ideal images. The third image with a linear polarization analyzer is the contour of a “trophy”. e) Experimental Stokes parameter S_3 of transmitted image under linear polarization illumination. It confirms the opposite handedness of “girl” and “snake” patterns.

linear polarization illumination, we can obtain three different polarization-dependent images, that is, “girl” (left-handedness), “snake” (right-handedness), and “trophy” (linear polarization). These vector-encoded images exhibit more information than the traditional holographic anti-counterfeiting featured by only one scalar image. To demonstrate the proof-of-concept, we design the phase profiles (Figure 4b) of two sparse holograms by following the GS algorithms and experimentally realize them by using the Nb_2O_5 nanobricks (see their SEMs in Figure 4c). Figure 4d shows the measured images under the different polarization analyzers. For a linear polarization analyzer, the “trophy” pattern is the vectorial mixture of the “girl” and “snake” patterns that can be observed from its spin image (Figure 4e) characterized by the Stokes parameter S_3 ($\equiv [I_{\text{RCP}} - I_{\text{LCP}}]/[I_{\text{RCP}} + I_{\text{LCP}}]$ ^[44]), where I_{RCP} and I_{LCP} are the intensity from the right-handed and left-handed components, respectively. Such a vector-featured image is not achievable in traditional anti-counterfeiting and enables strong anti-counterfeit protection due to its complexity and the difficulty in duplicating the random design at the nanoscale. Compared with the traditional holographic anti-counterfeiting technique that can only encode a scalar picture of the “trophy,” the vectorial anti-counterfeiting realizes data encoding by the “trophy” picture as well as their polarization profiles of two subpictures (i.e., “snake” and “girl”). It means that the correct information encoded in the vectorial anti-counterfeiting is a vector “trophy,” thereby providing an additional dimension of polarization for increasing the security of the encrypted data.

To distinguish the vectorial features of the image in real applications, one can also shine a polarization-tunable beam onto this ultra-channel hologram. If the incident light is elliptically polarized (i.e., $\sin\alpha\mathbf{e}_x + \sin\alpha\mathbf{e}_y$) as sketched in Figure 5a, one can observe an image of a mixture of the “girl” and “snake” patterns with their weights dependent on incident polarization. Figure 5b displays the experimentally captured images by addressing the parameter α . The gradual variation among three images confirms the vectorial feature, which is desired in this anti-counterfeiting technology.

In addition, through calculating the intensity encircled in “girl” and “snake” areas of these experimental images, we can indirectly derive the ratio $\gamma = I_{\text{RCP}}/I_{\text{LCP}}$, where I_{RCP} and I_{LCP} are the power of the right-handed and left-handed components of the incident light, respectively. Figure 5c shows the theoretical and experimental ratios, where the slight derivations under the CP ($\alpha = \pi/4$ or $3\pi/4$) illumination is caused by the inevitable background noise from the transmitted co-polarized light. It arises mainly from the transmitted co-polarized light and the environmental radiation, which generate the undesired but inevitable background noise. Similarly, the Stokes parameter S_3 ($= [1 - \gamma]/[1 + \gamma]$) of the incident light could also be obtained, as shown in Figure 5d, which manifests the handedness of the incident elliptical polarization light. Moreover, the total efficiency of this ultra-channel hologram is measured as high as 78.5%, indicating the robust performance of this Nb_2O_5 platform in developing functionalized nanodevices. A detailed introduction

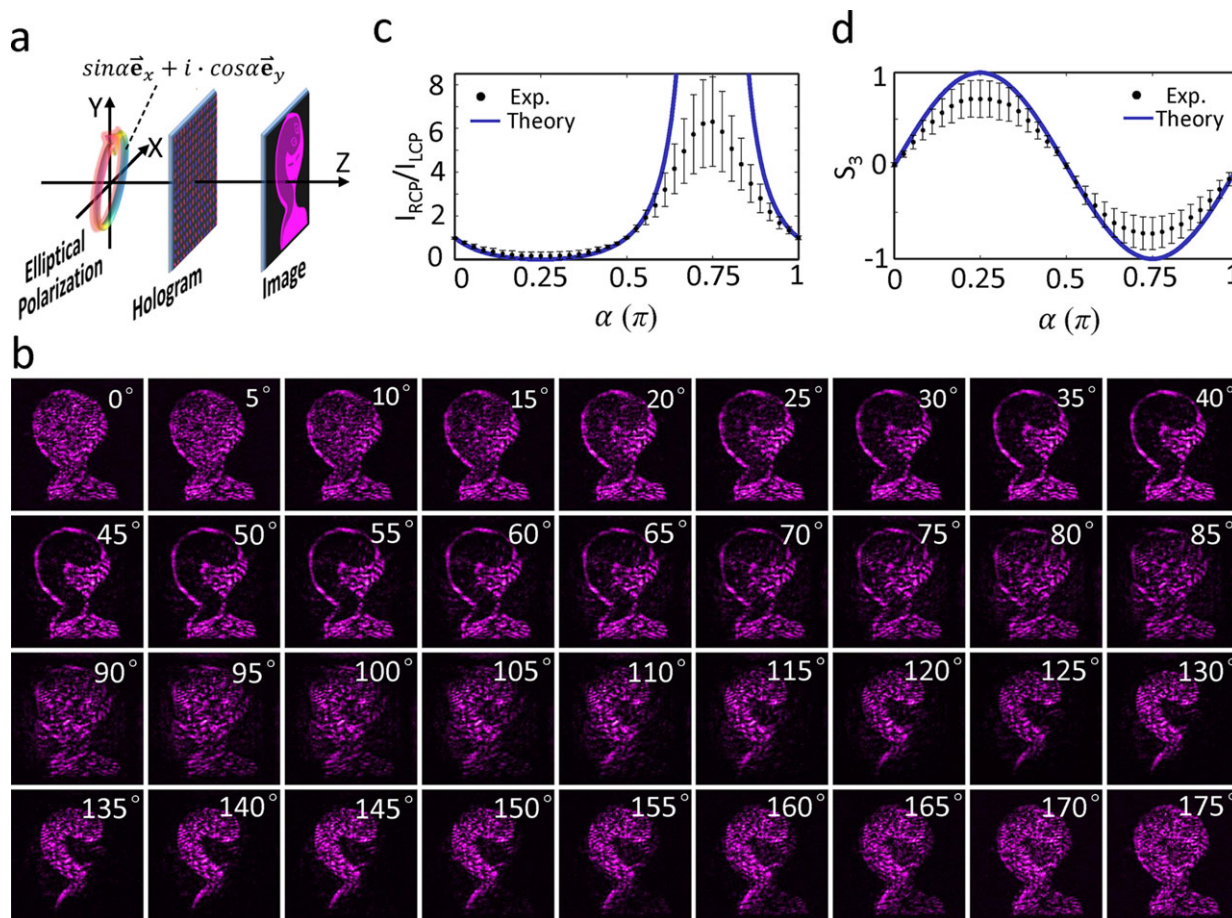


Figure 5. Optical vectorial anti-counterfeiting. a) Sketch for the demonstration of optical vectorial anti-counterfeiting. The elliptical polarization is controlled by using a linear polarizer and a quarter-waveplate, where α denotes the angle between the transmission axis of linear polarizer and the fast axis of quarter waveplate. b) Experimentally captured holographic images by addressing the angle α (labeled in white). c) The theoretical (curve) and experimental (dots) ratios $\gamma = I_{RCP}/I_{LCP}$, and d) Stokes parameter S_3 , in incident light.

about characterizing vectorial anti-counterfeiting can be found in Section 5, Supporting Information.

2.6. Discussions

The significance of our work is fourfold from the perspective of the high-efficiency ultraviolet metasurfaces. First, Nb_2O_5 can be integrated into photonic systems with the help of mature nanofabrication technology and our results affirm its feasibility in developing ultraviolet nanophotonics. Second, Nb_2O_5 exhibits a broader transparency window in the electromagnetic spectrum than TiO_2 and Si, thus allowing the development of planar nanodevices in the ultraviolet, visible, and infrared spectrums. Third, our transmissive metadvice confirms the possibilities to promote the miniaturization and planarization of other traditional ultraviolet bulky elements such as lenses and waveplates, thereby benefiting the potential applications of lithography and anti-counterfeiting at the spectrum of 350–400 nm. Finally, differing from the birefringent effects in traditional HWP and the electric dipole response in plasmonic nano-HWPs,^[45] the antiferromagnetic modes with the AMDs provide an alternative approach to

investigate the dielectric nano-HWPs. Although this antiferromagnetic mode is found in the Nb_2O_5 -based nanostructures at the ultraviolet wavelengths, it can also be extended to other material platforms (TiO_2 , Si, etc.) at the visible and infrared spectra (see Section 7, Supporting Information) because this operation is a mode scaling to match the electromagnetic interaction with the transparent dielectric nanostructures. In addition to offering the phase delay of π , the antiferromagnetic mode also provides a solution for high transmission under the x - or y -polarized incidence, as derived from the high-efficiency polarization conversion in both simulation and experiment. Although it is just an elementary work to understand the microscopic mechanism of the functionalized nano-structures by using antiferromagnetism, our report might excite intense researches to exploit the linking between antiferromagnetic modes and nano-optics.

3. Conclusion

In summary, we have demonstrated Nb_2O_5 -based dielectric meta-holograms that can achieve an efficiency of 79.6%. They can also produce high-quality images and provide a large angle of

view at the ultraviolet wavelength of 355 nm. Our ultra-channel meta-hologram is composed of two orthogonal channels that can generate three different images with polarization-dependent features. These are used to demonstrate the ultraviolet vectorial anti-counterfeiting. The optically induced antiferromagnetic modes hold the underlying physics of governing the polarization conversion in dielectric nano-HWPs, which offers a new paradigm for employing the microscopic magnetic phenomena to investigate nano-structures. The proposed Nb₂O₅ enriches the choices of materials for ultraviolet metadevices and flat optics and might facilitate the development of compact and unique optics for applications such as nano-photolithography, bio-imaging, and anti-counterfeiting.

Supporting Information

Supporting Information is available from the Wiley Online Library or from the author.

Acknowledgements

K.H., J.D., and H.S.L. contributed equally to this work. K.H. and H.L. conceived the idea. K.H. developed the theory, performed the simulations, and designed the holograms. J.D., S.Y., R.Y., and H.L. fabricated and characterized the samples. H.S.L. and K.H. built the experimental setup and implemented the optical measurement. K.H., J.T., and H.L. wrote the manuscript. H.L. and K.H. supervised the overall project. All authors discussed the results, did the data analysis, and commented on the manuscript. The authors would like to thank S. L. Teo and Doreen M. Y. Lai for the help in taking SEM images and Debbie H. L. Seng on surface analysis. K.H. thanks Prof. Lei Zhou for valuable suggestions about the electromagnetic theory. The authors acknowledge the financial support from the Agency for Science, Technology and Research (A*STAR) (Grant No. 162 15 00025). K.H. thanks the support from CAS Pioneer Hundred Talents Program, "The Fundamental Research Funds for the Central Universities" in China, and the National Natural Science Foundation of China (Grant Nos. 61875181 and 61705085).

Conflict of Interest

The authors declare no conflict of interest.

Keywords

antiferromagnetic resonance, high efficiency, niobium pentoxide, ultra-channel meta-holograms, ultraviolet metasurfaces

Received: October 31, 2018

Revised: March 1, 2019

Published online:

- [1] N. Yu, P. Genevet, M. A. Kats, F. Aieta, J.-P. Tetienne, F. Capasso, Z. Gaburro, *Science* **2011**, 334, 333.
- [2] P. Lalanne, S. Astilean, P. Chavel, E. Cambril, H. Launois, *Opt. Lett.* **1998**, 23, 1081.
- [3] Z. Bomzon, G. Biener, V. Kleiner, E. Hasman, *Opt. Lett.* **2002**, 27, 285.
- [4] N. K. Grady, J. E. Heyes, D. R. Chowdhury, Y. Zeng, M. T. Reiten, A. K. Azad, A. J. Taylor, D. A. R. Dalvit, H.-T. Chen, *Science* **2013**, 340, 1304.
- [5] X. J. Ni, N. K. Emani, A. V. Kildishev, A. Boltasseva, V. M. Shalaev, *Science* **2012**, 335, 427.
- [6] S. Sun, Q. He, S. Xiao, Q. Xu, X. Li, L. Zhou, *Nat. Mater.* **2012**, 11, 426.
- [7] L. Li, T. J. Cui, W. Ji, S. Liu, J. Ding, X. Wan, Y. Bo Li, M. Jiang, C.-W. Qiu, S. Zhang, *Nat. Commun.* **2017**, 8, 197.
- [8] G. Zheng, H. Mühlenbernd, M. Kenney, G. Li, T. Zentgraf, S. Zhang, *Nat. Nanotechnol.* **2015**, 10, 308.
- [9] A. Arbabi, Y. Horie, M. Bagheri, A. Faraon, *Nat. Nanotechnol.* **2015**, 10, 937.
- [10] L. Huang, X. Chen, H. Mühlenbernd, H. Zhang, S. Chen, B. Bai, Q. Tan, G. Jin, K.-W. Cheah, C.-W. Qiu, J. Li, T. Zentgraf, S. Zhang, *Nat. Commun.* **2013**, 4, 2808.
- [11] M. Khorasaninejad, W. T. Chen, R. C. Devlin, J. Oh, A. Y. Zhu, F. Capasso, *Science* **2016**, 352, 1190.
- [12] W. T. Chen, A. Y. Zhu, V. Sanjeev, M. Khorasaninejad, Z. Shi, E. Lee, F. Capasso, *Nat. Nanotechnol.* **2018**, 13, 220.
- [13] F. Aieta, M. A. Kats, P. Genevet, F. Capasso, *Science* **2015**, 347, 1342.
- [14] A. Arbabi, E. Arbabi, S. M. Kamali, Y. Horie, S. Han, A. Faraon, *Nat. Commun.* **2016**, 7, 13682.
- [15] Y. Ra'di, D. L. Sounas, A. Alu, *Phys. Rev. Lett.* **2017**, 119, 067404.
- [16] M. Khorasaninejad, K. B. Crozier, *Nat. Commun.* **2014**, 5, 5386.
- [17] X. Chen, L. Huang, H. Mühlenbernd, G. Li, B. Bai, Q. Tan, G. Jin, C. W. Qiu, S. Zhang, T. Zentgraf, *Nat. Commun.* **2012**, 3, 1198.
- [18] G. Li, S. Chen, N. Pholchai, B. Reineke, P. W. H. Wong, E. Y. B. Pun, K. W. Cheah, T. Zentgraf, S. Zhang, *Nat. Mater.* **2015**, 14, 607.
- [19] Y. Yang, W. Wang, A. Boulesbaa, I. I. Kravchenko, D. P. Briggs, A. Poretzky, D. Geohagan, J. Valentine, *Nano Lett.* **2015**, 15, 7388.
- [20] E. Maguid, I. Yulevich, D. Veksler, V. Kleiner, M. L. Brongersma, E. Hasman, *Science* **2016**, 352, 1202.
- [21] K. Huang, Z. Dong, S. Mei, L. Zhang, Y. Liu, H. Liu, H. Zhu, J. Teng, B. Luk'yanchuk, J. K. Yang, *Laser Photonics Rev.* **2016**, 10, 500.
- [22] D. Lin, P. Fan, E. Hasman, M. L. Brongersma, *Science* **2014**, 345, 298.
- [23] L. Wang, S. Kruk, H. Tang, T. Li, I. Kravchenko, D. N. Neshev, Y. S. Kivshar, *Optica* **2016**, 3, 1504.
- [24] S. Wang, P. C. Wu, V.-C. Su, Y.-C. Lai, M.-K. Chen, H. Y. Kuo, B. H. Chen, Y. H. Chen, T.-T. Huang, J.-H. Wang, R.-M. Lin, C.-H. Kuan, T. Li, Z. Wang, S. Zhu, D. P. Tsai, *Nat. Nanotechnol.* **2018**, 13, 227.
- [25] S. Colburn, A. Zhan, A. Majumdar, *Sci. Adv.* **2018**, 4, eaar2114.
- [26] K. Huang, H. Liu, F. J. Garcia-Vidal, M. Hong, B. Luk'yanchuk, J. Teng, C.-W. Qiu, *Nat. Commun.* **2015**, 6, 7059.
- [27] K. Huang, H. Liu, G. Si, Q. Wang, J. Lin, J. Teng, *Laser Photonics Rev.* **2017**, 11, 1700025.
- [28] Y. Deng, X. Wang, Z. Gong, K. Dong, S. Lou, N. Pégard, K. B. Tom, F. Yang, Z. You, L. Waller, J. Yao, *Adv. Mater.* **2018**, 30, 1802632.
- [29] L. Zhang, S. Mei, K. Huang, C.-W. Qiu, *Adv. Opt. Mater.* **2016**, 4, 818.
- [30] A. I. Kuznetsov, A. E. Miroshnichenko, M. L. Brongersma, Y. S. Kivshar, B. Luk'yanchuk, *Science* **2016**, 354, aag2472.
- [31] W. Liu, Y. S. Kivshar, *Philos. Trans. R. Soc., A* **2017**, 375, 20160317.
- [32] R. A. Rani, A. S. Zoofakar, A. P. O'Mullane, M. W. Austin, K. Kalantar-Zadeh, *J. Mater. Chem. A* **2014**, 2, 15683.
- [33] R. Ghosh, M. K. Brennaman, T. Uher, M.-R. Ok, E. T. Samulski, L. McNeil, T. J. Meyer, R. Lopez, *ACS Appl. Mater. Interfaces* **2011**, 3, 3929.
- [34] J.-C. Su, C.-L. Lu, C.-W. Chu, *Appl. Opt.* **2009**, 48, 4942.
- [35] T. Blanquart, J. Niinistö, M. Heikkilä, T. Sajavaara, K. Kukli, E. Puukilainen, C. Xu, W. Hunks, M. Ritala, M. Leskelä, *Chem. Mater.* **2012**, 24, 975.
- [36] W. Luo, S. Sun, H.-X. Xu, Q. He, L. Zhou, *Phys. Rev. Appl.* **2017**, 7, 044033.
- [37] P. Grünberg, R. Schreiber, Y. Pang, M. Brodsky, H. Sowers, *Phys. Rev. Lett.* **1986**, 57, 2442.

- [38] L. Šmejkal, Y. Mokrousov, B. Yan, A. H. MacDonald, *Nat. Phys.* **2018**, *14*, 242.
- [39] P. Němec, M. Fiebig, T. Kampfrath, A. V. Kimel, *Nat. Phys.* **2018**, *14*, 229.
- [40] N. Liu, S. Mukherjee, K. Bao, L. V. Brown, J. Dorfmueller, P. Nordlander, N. J. Halas, *Nano Lett.* **2012**, *12*, 364.
- [41] A. E. Miroshnichenko, B. Luk'yanchuk, S. A. Maier, Y. S. Kivshar, *ACS Nano* **2012**, *6*, 837.
- [42] S. Lepeshov, Y. S. Kivshar, *ACS Photonics* **5**, 2888, **2018**.
- [43] K. Huang, F. Qin, Hong Liu, H. Ye, C. W. Qiu, M. Hong, B. Luk'yanchuk, J. Teng, *Adv. Mater.* **2018**, *30*, 1704556.
- [44] M. Born, E. Wolf, *Principles of Optics: Electromagnetic Theory of Propagation, Interference and Diffraction of Light*. Cambridge University Press, Cambridge **1999**.
- [45] L. Huang, X. Chen, H. Mühlenbernd, G. Li, B. Bai, Q. Tan, G. Jin, T. Zentgraf, S. Zhang, *Nano Lett.* **2012**, *12*, 5750.